Flow and shear behavior in the edge and scrape-off layer of L-mode plasmas in National Spherical Torus Experiment

Y. Sechrest,[1] T. Munsat,[1] D. A. D'Ippolito,[2] R. J. Maqueda,[3] J. R. Myra,[2] D. Russell,[2] and S. J. Zweben[3]
[1]*Department of Physics, University of Colorado, Boulder, Colorado 80309, USA*
[2]*Lodestar Research Corporation, Boulder, Colorado 80301, USA*
[3]*Princeton Plasma Physics Laboratory, Princeton, New Jersey 08540, USA*

(Received 1 November 2010; accepted 13 December 2010; published online 10 January 2011)

Fluctuations in the edge and scrape-off layer (SOL) of L-mode plasmas in the National Spherical Torus Experiment [Kaye *et al.*, Phys. Plasmas **8**, 1977 (2001)] as observed by the gas puff imaging (GPI) diagnostic are studied. Calculation of local, time resolved velocity maps using the hybrid optical flow and pattern matching velocimetry code enables analysis of turbulent flow and shear behavior. Periodic reversals in the direction of the poloidal flow near the separatrix are observed. Also, poloidal velocities and their radial shearing rate are found to be well correlated with the fraction of D_α light contained in the SOL, which acts as a measure of turbulent bursts. The spectra of GPI intensity and poloidal velocity both have a strong feature near 3 kHz, which appears to correspond with turbulent bursts. This mode exhibits a poloidal structure with poloidal wavenumber of 7.7 m^{-1} for GPI intensity and 3.4 m^{-1} for poloidal velocity, and the poloidal velocity fluctuations near 3 kHz remain coherent over length scales in excess of the turbulent scales. Furthermore, recent SOL turbulence simulations find a parameter regime that exhibits periodic bursty transport and shares many qualitative similarities with the experimental data. Strong correlations between the shearing rate and the turbulent bursts are observed for time periods of ~ 2 ms, but the relationship is complicated by several factors. Finally, measurements of the radial profiles of the Reynolds shear stresses are reported. These radial profiles exhibit many similarities for several shots, and a region with positive radial gradient is seen to be coincident with local flow shear. © *2011 American Institute of Physics*. [doi:10.1063/1.3533435]

I. INTRODUCTION

The problem of turbulent transport is ubiquitous in magnetic confinement fusion devices, and is often cited among the primary performance limitations of these devices. One of the driving processes behind this anomalous transport is believed to be the drift wave instability. Recently, focus has been given to the interaction of drift waves with large scale sheared flows. Theoretical predictions[1–3] and experimental results[4–6] suggest that zonal flows can be self-generated by the turbulence through torque supplied by the turbulent shear stresses. These zonal flows are driven by radially localized, toroidally, and azimuthally symmetric electrostatic potential structures that drive time varying sheared $E_r \times B_t$ flows, where E_r is the radial electric field and B_t is the toroidal magnetic field. In some theoretical models, these sheared flows break up turbulent eddies, and so may act to suppress the turbulent transport. Alternatively, the turbulent shear stresses can be thought to transfer energy from the turbulence to the large scale flow, and again the turbulence and associated transport are consequently suppressed. Thus, drift wave turbulence and zonal flows are believed to form a self-regulating system in which turbulence-generated zonal flows act to control the turbulence amplitude.

The interaction between drift wave turbulence and zonal flows makes it clear that flow organization can play an important role in magnetic confinement devices. Acknowledging this fact, several groups have recently sought to measure the two-dimensional (2D) flow properties in tokamaks and laboratory plasma devices. Of particular note are the 2D velocity map studies by the DIII-D group using beam emission spectroscopy (BES),[7] the C-Mod group using gas puff imaging (GPI),[8] and the controlled shear decorrelation experiment (CSDX) group using fast camera imaging of visible light.[9] Each group employs a time-delay estimation (TDE) technique[10] to derive a 2D velocity field, which can then be analyzed to yield properties of the flow including shear and turbulence stresses.

The BES study on DIII-D produced time resolved flow fields with ~ 1 cm spatial resolution, at 4×7 points spatially, and time resolution of 20 μs. The analysis of these measurements has provided observations of low frequency zonal flows,[11] and important evidence of geodesic acoustic modes (GAMs),[7,12] a higher frequency branch of zonal flow. The C-Mod group used TDE techniques to infer time-averaged velocity fields for edge turbulence, showing a strong poloidal rotation inside the separatrix. Their results, however, were limited to one ~ 1 ms time-averaged flow field per shot, with ~ 0.5 cm resolution. Finally, the CSDX team has used fast camera imaging to derive velocity profiles for the study of shear flows in the cylindrical helicon plasma device.[9]

Recently, Zweben *et al.*[13] reported on the observation of "quiet periods" in the National Spherical Torus Experiment[14] (NSTX) edge prior to the L-H transition. These quiet periods were observed with the GPI diagnostic, and they found that the GPI D_α light emission during these periods resembled

that of H-mode. The quiet periods occurred at a frequency of ~3 kHz, and were correlated with changes in the direction of the poloidal flow. They also found that the dimensionless poloidal shearing values were correlated with the quiet periods. However, a trigger for the L-H transition again proved to be elusive.

In this work, we analyze the same database of shots as Zweben *et al.*[13] However, we use a hybrid optical flow and pattern matching velocimetry (HOP-V) technique[15] to derive 2D velocity fields using GPI data from the NSTX edge region. This technique yields time resolved velocity fields with a spatial resolution of ~1.5 cm, at 16×16 spatial points, and time resolution of 3.5 μs. Using the derived velocity fields and GPI data we report on three main results: (1) detailed characterization of space and time evolution of zonal flow features, (2) calculation of turbulence shear stress and its radial profiles, and (3) relationship between zonal flow and turbulent bursts.

This article begins with a review of the GPI diagnostic (Sec. II) and the HOP-V velocimetry code (Sec. III). Section IV discusses general flow properties observed in a series of L-mode discharges, and is followed by observations of quiet periods and periodic behavior in Sec. V. Finally, Sec. VI presents analysis of turbulence quantities and flows including shear and Reynolds stresses.

II. GPI

A brief review of the GPI diagnostic on NSTX is included here, however we refer the reader elsewhere for a more detailed discussion.[16,17] The GPI diagnostic is a method for imaging turbulent fluctuations in the edge of hot magnetically confined plasmas. A gas manifold located at the edge of the device discharges a gas puff into the plasma, and visible line emission from the cloud is then imaged with a fast framing camera. The GPI system on NSTX used for this study images visible D_α line emission at 656 nm from a deuterium gas puff with the camera view approximately aligned with the local magnetic field. Thus the 2D structure of the turbulence is resolved in the poloidal plane.

In the collisional radiative approximation and ignoring photons resulting from molecular processes, the intensity of the line emission has the following form:

$$S = n_0 f(n_e, T_e) A. \tag{1}$$

Here, n_0 is the local density of the neutral ground state, A is the radiative decay rate for the transition, and the function $f(n_e, T_e)$ gives the ratio of the density of the upper state of the transition to the ground state as a function of local electron density n_e and temperature T_e. The functional dependence for the geometry and typical edge parameters of NSTX ($T_e \simeq 10$ eV, $n_e \simeq 10^{18}$ m^{-3}) is $S \propto n_e^{0.9} T_e^{1.0}$.[18,19] However, the exponents vary with n_e and T_e. This dependence is consistent with the measured radial profiles of D_α emission.

The GPI field of view is centered approximately 20 cm above the outer midplane of the machine near the separatrix, and covers a roughly 25 cm by 25 cm area with the horizontal and vertical axes of the camera images aligned with the radial and poloidal directions, respectively. The pixel resolution of the diagnostic is ~4 mm, and the spatial resolution of the emission cloud set by the curvature of the field lines is $\leq$1 cm. Thus, having typical correlation lengths of ~3–5 cm, the turbulent structures in the edge of the device are adequately resolved.

For this study images were captured using two Phantom 7.3 fast cameras from Vision Research. The cameras are set to view the same image, then image captures are alternated between the two cameras to achieve the highest possible frame rate. In this way, images are captured at 285 000 frames/s (3.5 μs/frame), with 3 μs/frame exposure. With the current GPI system it is possible to record ~17 000 frames per shot (~50 ms), limited by the duration of the gas puff, at a resolution of 64×64 pixels.

III. HYBRID OPTICAL FLOW ALGORITHM

To analyze plasma flow from the GPI image sequences we use a two part velocity extraction algorithm. This technique, described in detail in Ref. 15, combines an optical flow approach with a pattern matching technique to overcome many of the limitations of the techniques applied individually, and is therefore named the HOP-V algorithm. A brief review of the general concepts is included below.

First, an estimate of the velocity field is obtained from the optical flow component, which has the benefit of requiring no arbitrary initial conditions. The technique attempts to solve for the velocity field that maps one image to the next with the constraint that local, intensity structures remain approximately constant between frames. That is to say, intensity structures in the images are presumed to translate, but not appear or disappear. Thus, the algorithm seeks the two-component velocity field, $\mathbf{v}=(v_x, v_y)$, that satisfies

$$I(x,y,t) = I(x + v_x \Delta t, y + v_y \Delta t, t + \Delta t), \tag{2}$$

where I is the image brightness and Δt is small such that the displacement can be approximated to first order. Differentiating Eq. (2) yields the continuity equation for image brightness with the assumption of divergence free flow, which must then be solved for each image pixel to obtain the velocity field for the whole image. The HOP-V implementation accomplishes this by recasting the continuity equation as a matrix equation, decomposing the scalar field of each velocity component using a family of 2D wavelet basis functions. The resulting equation can then be solved via matrix inversion to yield the full velocity field with spatial and temporal resolution equal to the supplied image sequence.

The optical flow method is, however, not without limitations. The principal limitation is the algorithm's inability to detect motion along a line of constant intensity, and is commonly referred to as the "aperture problem." In practice this hinders the usefulness of the algorithm, and complicates interpretation of results. It is also possible for fast moving structures to be "lost" or have significantly underestimated velocities when the ratio of displacement to the structure's full width at half maximum is $\geq$1. To overcome these limitations, a second pass is performed that employs a pattern matching approach.

Given a pair of sequential images, the basic approach of the pattern matching component is to first subdivide the entire first image into a number of smaller blocks or tiles consisting of several pixels. Each tile is then correlated with a subsection of the subsequent image in a 2D optimization search. The velocity vector for the tile is then calculated from the time between frames Δt and the displacement vector that optimizes the correlation. In this manner a velocity vector is derived for each tile and each image, and a 2D velocity field is obtained with the temporal resolution of the initial image sequence and at a spatial resolution reduced by the ratio of the initial image resolution to the size of a tile.

In practice, the optimization process is done by the minimization of a global error function defined as

$$F = \left(\sum_{\text{tiles}} F_D \right) + \lambda F_s. \tag{3}$$

F_D encompasses the correlation optimization, and is essentially a tile-integrated intensity difference calculated between a tile and the associated section of the subsequent image. Thus, this technique also relies on the assumption of locally constant brightness. F_s is used to impose a smoothness constraint on the velocity field, and the relative weighting between the two functions can be adjusted by the free parameter λ. The optimization process is also carried out iteratively with several passes per tile resolution and iterations at multiple tile resolutions. For the analysis in Secs. IV–VI, images of 64×64 pixels are first broken into tiles of 8×8 pixels, and then, after three iterations at this resolution, the tile size is decreased to 4×4 pixels and another three iterations are done.

Unlike the optical flow technique, the pattern matching algorithm requires an "initial guess" for the velocity field to act as a starting point for the optimization. In the pattern matching technique, however, velocity vectors are not constrained to lie along the intensity gradient. Furthermore, the speed of trackable structures is only limited by the breadth of the spatial optimization search. In the HOP-V algorithm the arbitrariness of the initial guess is circumvented by using the optical flow velocity field as an input. Therefore, by using the two techniques in succession the HOP-V algorithm is free of arbitrary initial conditions, and produces results that are more accurate than the optical flow technique alone. The resulting velocity field tracks the apparent motion of intensity structures in the image, which we take to be indicative of the underlying plasma flow. However, due to the dependence of line emission on local plasma parameters and subtleties of the optical estimation of flow, the connection between observed motion and plasma flow is potentially quite complicated. Future work will seek to elucidate this issue by directly comparing HOP-V velocity fields to known quantities in simulation data sets.

The HOP-V code has been tested on several image sets with imposed velocities.[15] Velocities were accurately recovered for simple translations as well as sheared flows, however, accuracy was seen to degrade when velocities reached 7 pixels/frame (~7.5 km/s for NSTX GPI geometry).

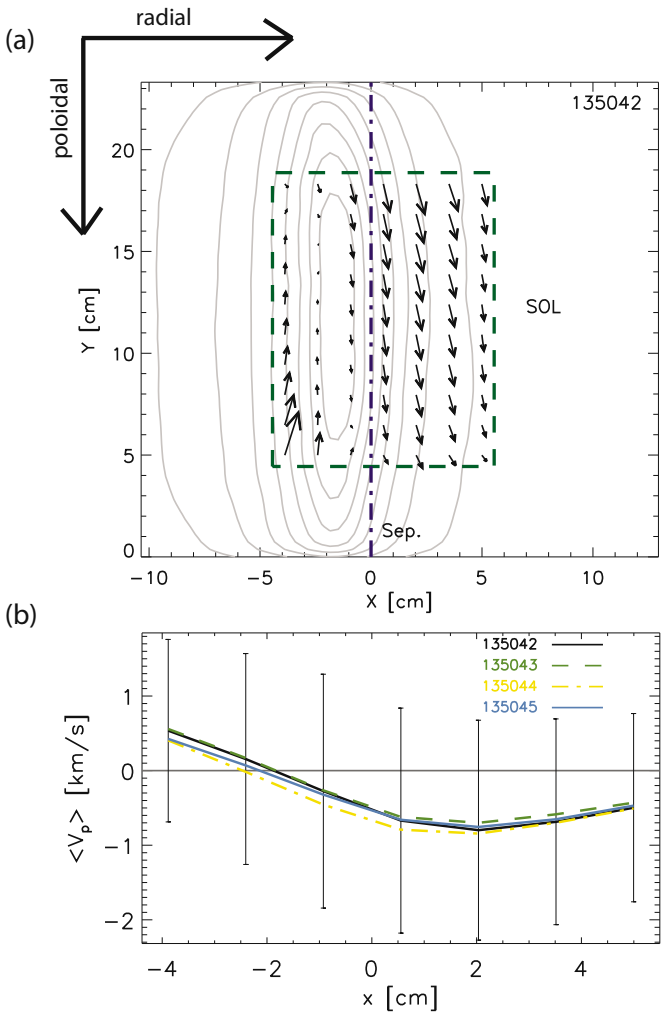

FIG. 1. (Color online) (a) Time-averaged velocity field superimposed on time-averaged GPI intensity contours (gray contours). The separatrix is indicated by the dot-dashed line, and the cropped field of view is indicated by the dashed box. The maximum time-averaged velocity magnitude for the cropped region is 1.5 km/s, while the maximum instantaneous velocity magnitude is 7.4 km/s. The $+x$ direction is radially outward. (b) Radial profiles of time-averaged poloidal flow for 10.5 μs time periods preceding the L-H transition. Root-mean-square values of the fluctuating velocity are shown for shot 135042.

IV. GENERAL CHARACTERISTICS OF THE FLOW

All of the shots discussed in this paper (135021–23 and 135041–46) have a GPI image size of 64×64 pixels, and the final iteration of the HOP-V algorithm correlates tiles of 4×4 pixels. This produces a 16×16 point velocity field at the temporal resolution of the image sequence as illustrated by Fig. 1(a). In the figure the time-averaged velocity field for a period of approximately 10 ms during L-mode operation is superimposed upon time-averaged contours of GPI intensity. The GPI intensity falls off near the top and bottom of the view due to vignetting of the optics and the limited size of the GPI emission cloud. The velocity field has been cropped to an approximately 10.4 cm $\times$ 14.8 cm (7×10 points) section in the center of the GPI field of view to avoid these edge effects. Also, due to the emission profile of the GPI gas puff, the intensity fluctuations outside this boxed region are not high enough to consistently yield strong correlations for the

HOP-V algorithm, and as a result velocity data from these regions are often not reliable. All analysis (poloidal averaging, etc.) in this work will be limited to the boxed region of Fig. 1(a). The approximate location of the separatrix (dot-dashed line) is determined from a standard equilibrium model using magnetic measurements and Thomson scattering profiles, and is uncertain to ±2 cm. The exact location of the separatrix is not, however, a critical aspect of the analysis. The radial position is displayed relative to the separatrix position.

Figure 1 serves to illustrate some general characteristics of the observed flow. In movies of the GPI signal (viewable in the multimedia section of Zweben *et al.*[13]), intensity structures ("blobs") are typically seen to move with positive velocity (upward, in the electron diamagnetic direction) in the inner region ($x \approx -5-0$ cm), while slowly moving radially outward. As the structures cross the separatrix and move into the scrape-off layer (SOL), their poloidal velocity reverses direction, and they move downward (in the ion diamagnetic direction). Figure 1(b) shows a similar pattern with negative average velocities outside the separatrix, while flow reversals tend to average to zero near the separatrix. Average velocities are on the order of 1.5 km/s poloidally and 0.5 km/s radially, and instantaneous velocities can be significantly higher, as discussed below. Several centimeters inside the separatrix, the average poloidal velocities, are positive. This suggests the presence of radial flow shear across the separatrix in the average shown. A similar pattern in the time-averaged flow field is seen in shots 135041–135046, and similarities can be seen in Fig. 1(b). In addition most all shots show a clear downward average flow outside the separatrix. "Error bars" in Fig. 1(b) indicate rms levels of the fluctuating poloidal velocity for shot 135042, so it can be seen that the velocity fluctuations are on the order of the mean flow values.

To illustrate temporal behavior, time traces for normalized GPI intensity, poloidal velocity, and radial velocity are shown in Fig. 2 (shot 135042, $t \approx 0.241-0.243$ s). In the figure, each trace represents a poloidal average, localized radially approximately 1 cm inside the separatrix, which is near the time-averaged GPI intensity maximum. Gray outlines of V_p and V_r indicate the level of uncertainty in these values assuming random, statistically independent uncertainties in the individual velocity measurements of 0.5 km/s (~0.5 pixel/frame). In the averages shown, the level of uncertainty is ~0.15 km/s.

The GPI intensity is normalized by subtracting from each pixel its mean value taken over the full 17000-frame exposure and then dividing by the mean, so a value of 1.0 indicates a fluctuation which is on the order of the mean value. Typically, poloidal velocities are seen to range between ±10 km/s, and mean poloidal flows exhibit a pattern of large amplitude bursty oscillations. Radial velocities are generally on the order of a few kilometers per second, and can approach the minimum threshold of measurable velocities of ~0.5 km/s. As mentioned previously, the poloidal velocity changes from being predominantly positive inside the separatrix to negative in the SOL. Near the separatrix, the poloidal flow is seen to fluctuate around zero with periodic reversals.

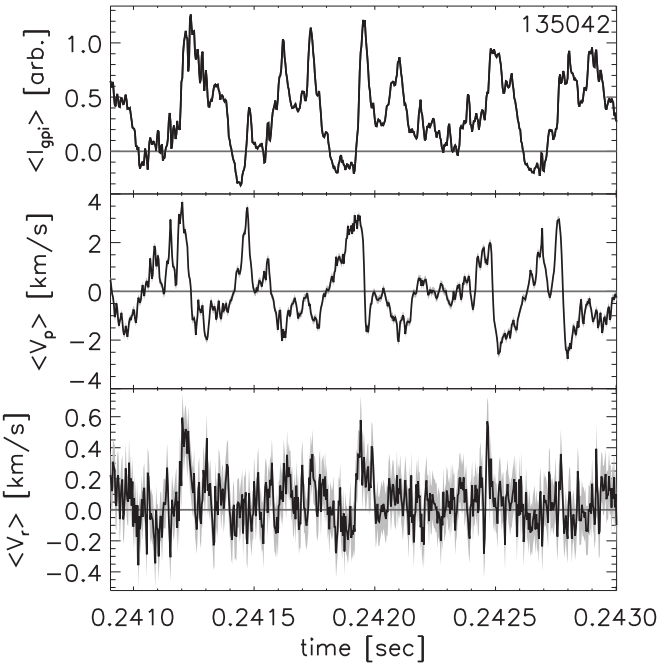

FIG. 2. Normalized GPI intensity (top), poloidal velocity (middle), and radial velocity (bottom) ~1 cm inside the separatrix. All traces represent poloidally averaged quantities from shot 135042.

V. CHARACTERIZATION OF ~3 kHz OSCILLATIONS

GPI recordings of nine shots in which the L-H transition was captured in the GPI sequence have been analyzed for this study. These shots have been recently analyzed in Zweben *et al.*,[13] and the L-mode sections of these shots are the focus of this paper. Intervals of time traces for the turbulence and flow quantities of all shots exhibit distinct periodic oscillations/bursts. Of the quantities that exhibit this pattern, the relative intensity of D_α light outside the separatrix (F_{sol}, developed in Zweben *et al.*[13]) has been used to measure H-mode-like behavior, and can be used as an indicator for other oscillating properties. The quantity F_{sol} is defined as the fraction of the total GPI intensity contained in the SOL, and is plotted in Fig. 3(a) along with poloidal velocity traces at three radial locations (chosen inside, at, and outside the separatrix, shown in Fig. 3(b)–3(d), respectively). A spike in F_{sol} corresponds to intensity structures (blobs) passing into the SOL. In this way F_{sol} essentially acts as a gauge for turbulent bursts. Periods of low F_{sol} have previously been identified as quiet periods or H-mode-like,[13] and are indicated in Fig. 3 by the vertical gray bars.

Low frequency components of F_{sol} between 0 and 1 kHz have been removed from the filtered F_{sol} trace in Fig. 3(a), and the gray bars indicate where the filtered F_{sol} is below 0.16 (arbitrarily chosen as a rough guide to distinguish "high" versus "low"). Periodic behavior in F_{sol} is easily discernible; the large scale oscillations between $t=0.241$ and 0.243 s have a frequency of ~3 kHz. However, this periodicity in F_{sol} is somewhat irregular and appears to be intermittent.

The intermittency of this ~3 kHz feature is demonstrated by the spectrogram of F_{sol} shown in Fig. 4. The spectrogram covers the entire recorded L-mode portion of shot

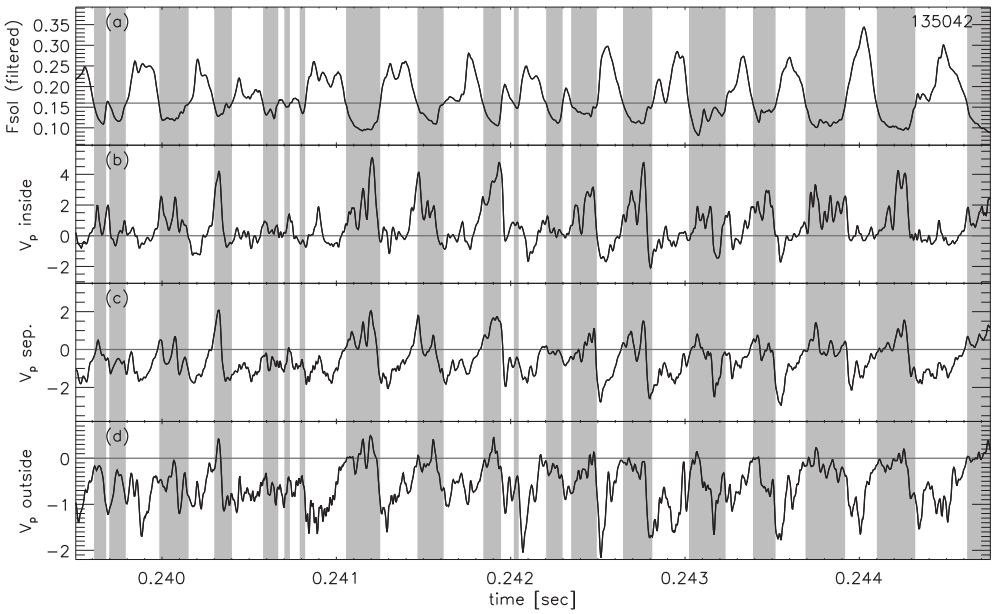

FIG. 3. (a) Traces from shot 135042 of F_{sol} filtered, and (b) poloidally averaged poloidal velocity inside, at (c), and (d) outside the separatrix. F_{sol} filtered has had the low frequency components above zero frequency and below 1 kHz removed. Gray bars indicate time periods where F_{sol} filtered is below 0.16.

135042 with a window of 256 time points (~0.9 ms), giving roughly 1.1 kHz resolution. In constructing the spectrogram, a sliding fast-Fourier-transform is used with Hanning windowing and 75% overlap. The spectrogram shows a dominant mode that appears sporadically near 3 kHz. This mode fluctuates between 2 and 4 kHz, and tends to have relatively stationary durations of ~1–2 ms. These characteristics are directly apparent in Fig. 3(a) as well. Periodic bursts in F_{sol} and poloidal velocity at about 2.5 kHz start near 0.2410 s and are clearly observable until 0.2420 s, then after 0.2425 s this periodicity revives. During these time periods, Large scale fluctuations of the poloidal velocity appear to be about 180° out of phase with F_{sol}.

Shots 135021 and 135041–44 each have a feature in the spectrogram of F_{sol} with similar qualities to shot 135042. This feature is generally centered between 2 and 5 kHz, and fluctuates within a ~2 kHz range around this center value. The feature is stationary for durations of 1–2 ms such as with shot 135042. The other shots (135022–23 and 135045–46) show a similar feature. However it is less distinct in these shots and often does not persist through the entire shot.

The measured poloidal velocities shown in Fig. 3 also exhibit high correlation with F_{sol}. Periods of low F_{sol} (quiet periods) are correlated with positive peaks in poloidal velocity inside the separatrix, and peaks in F_{sol} correspond to periods of nearly zero flow. Outside the separatrix the reverse is true, with poloidal velocities tending toward zero during quiet periods and peaking negative during turbulent bursts. The correlation coefficient at each of the three locations chosen between F_{sol} and V_p for the time period shown is ~0.6.

Correlation values between successive images (which measure the "tracking quality" of the velocimetry algorithm) for velocity vectors in the SOL tend to decrease during quiet periods, but a majority of the vectors remain above an 80% correlation threshold. Therefore, it appears that the SOL velocities are not simply an artifact of low GPI signal in the SOL.

Reversals in poloidal velocity can be seen at the separatrix, with positive velocities observed during quiet periods, switching sign as F_{sol} rises. The correlation between these quantities suggests a relationship between the poloidal flow and the turbulent bursts. This may indicate that some feature of poloidal flows acts to control the turbulence, or that the flow is generated by the release of blobs. A causal relationship is, however, unclear at this point, and begs further inquiry.

The spatial structure of the ~3 kHz mode was analyzed by first applying a bandpass filter to the GPI signal around this dominant frequency. For $t \approx 0.241-0.243$ s of shot 135042, the filter is used to select a single mode near 2.4 kHz, corresponding to the frequency of peak spectral power for GPI intensity ~1 cm inside the separatrix. With the applied filter, a rotating mode is clearly observed which exhibits long poloidal wavelength and radial size greater than 4 cm. The mode appears in the images as an oscillating band

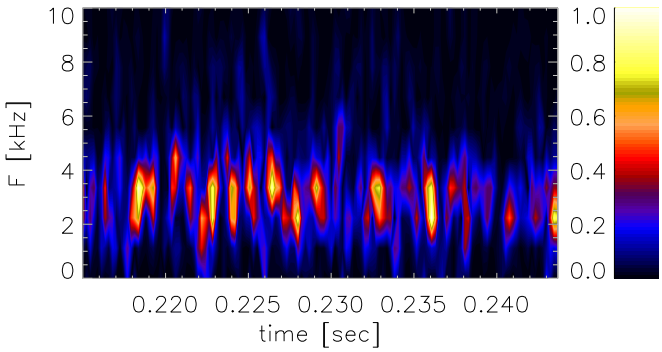

FIG. 4. (Color online) Spectrogram of F_{sol} for the L-mode portion ($t \approx 0.215-0.245$) of shot 135042 plotted with a linear color scale.

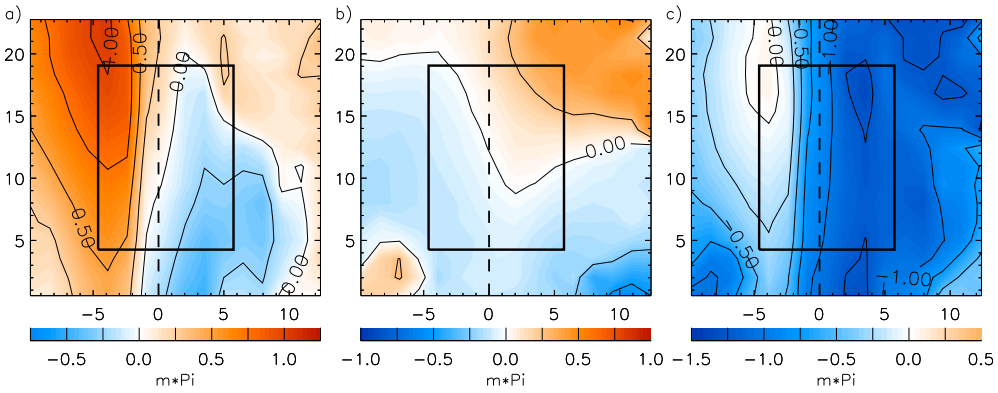

FIG. 5. (Color online) Map of phase differences of ~2.4 kHz fluctuations for: (a) GPI signal with reference GPI signal, (b) v_{pol} with reference v_{pol}, and (c) GPI signal with v_{pol}. Reference signals are at $x \approx 0$ cm, $y \approx 11$ cm. Plots (a) and (c) have had the phase discontinuity remapped so that the contour plots appear smooth. Plots cover the time range $t \approx 0.241-0.243$ ms of shot 135042. The dashed-line indicates the separatrix.

centered 0.5 cm inside the separatrix with a radial width of ~2 cm that spans the full GPI view in the poloidal direction.

The spatial structure of this mode is illustrated by the X-Y phase maps shown in Fig. 5. Figures 5(a) and 5(b) show the X-Y map of the cross-phase calculated from the cross-spectral density function of raw GPI signal (poloidal velocity) at each point with a reference signal. Figure 5(c) shows the cross-phase of GPI signal with poloidal velocity. The GPI fluctuations [Fig. 5(a)] undergo a phase shift of nearly π between locations inside and outside the separatrix. However, in the poloidal direction at $x \approx -1$ cm the phase changes approximately linearly with position, and over the full GPI range it changes by $\sim \pi/2$. The poloidal wavenumber k_p can be obtained by a linear fit to the phase shift versus y, resulting in $k_p = 7.7$ m^{-1} at $x \approx -1$ cm. The poloidal velocity fluctuations [Fig. 5(b)] at $x \approx -1$ cm have a significantly longer (but not infinite) wavelength in the poloidal direction, with $k_p = 3.4$ m^{-1}. The phase of the poloidal velocity also does not show the strong radial dependence seen in the GPI intensity.

Figure 6 shows one-dimensional plots of phase of the ~3 kHz oscillations versus spatial coordinate for periods of shots 135042–135045 where a rotating mode is visible in the bandpass filtered data. For the radial dependence, the data are averaged poloidally before the phase is calculated, and the phase versus y is taken ~1 cm inside the separatrix. The phase of the GPI signal for these periods changes rapidly from $x = -2$ to $x = 0$ cm, while in the poloidal direction the phase has an approximately linear dependence on position. From this linear dependence it can be seen that the poloidal wavelengths are long, with poloidal wavenumbers on the order of 10 m^{-1}. As a function of radius, the phase of the poloidal velocity remains small, but becomes more negative with increasing radius. This means that the 3 kHz flow oscillations in the SOL lead the flow inside the separatrix, and this lag time is ~15 μs. For the poloidal direction, wavenumbers for the poloidal velocity are typically smaller than the GPI signal by about a factor of 2.

Poloidal correlation lengths for the ~3 kHz feature can be estimated from the coherence function between two signals. Figure 7 shows the coherence and phase versus frequency for poloidal velocity signals of shots 135042–44. The coherence function for two points separated by ~12 cm in the poloidal direction is calculated from the cross-spectral and autospectral density functions as outlined in section 11.6 of Bendat and Piersol.[20] The cross-spectral and autospectral density functions are estimated by ensemble averaging estimates from 14 time blocks of 512 time points (1.8 ms) each. Each shot shows a mode near 2.8 kHz that maintains high coherence and small phase difference over ~12 cm. All shots analyzed exhibit a peak in the coherence function in the range of 2–4 kHz with phase differences less than $\pi/4$.

Figure 8 shows the coherence as a function of poloidal separation for poloidal velocity signals. Coherence functions are estimated for increasing poloidal separations, and the figure compares the coherence of the 2.8 kHz mode to the average coherence value for the turbulence between 20

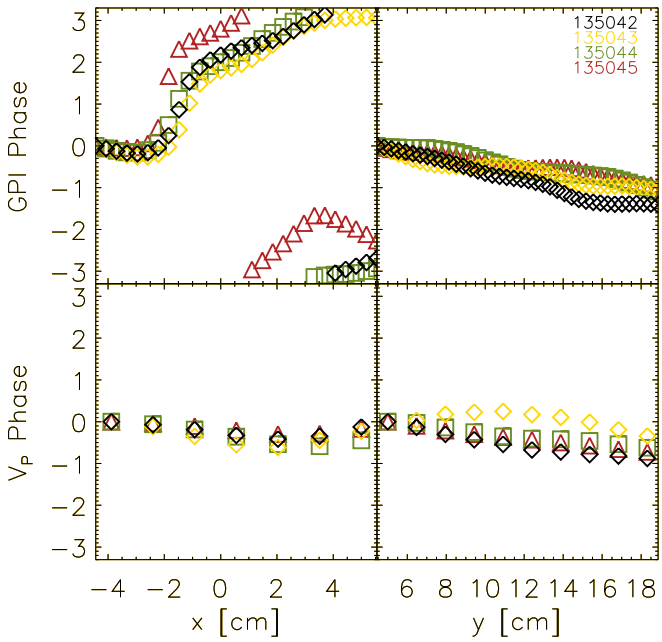

FIG. 6. (Color online) Phase of ~3 kHz mode plotted vs spatial coordinates for GPI signal and poloidal velocity for periods of shots 135042–135045 with "rotating mode" visible in bandpass filtered. Time periods are 512 frames (1.8 ms) and begin at: 135042 $t = 0.241$, 135043 $t = 0.238$, 135044 $t = 0.230$, and 135045 $t = 0.236$ s.

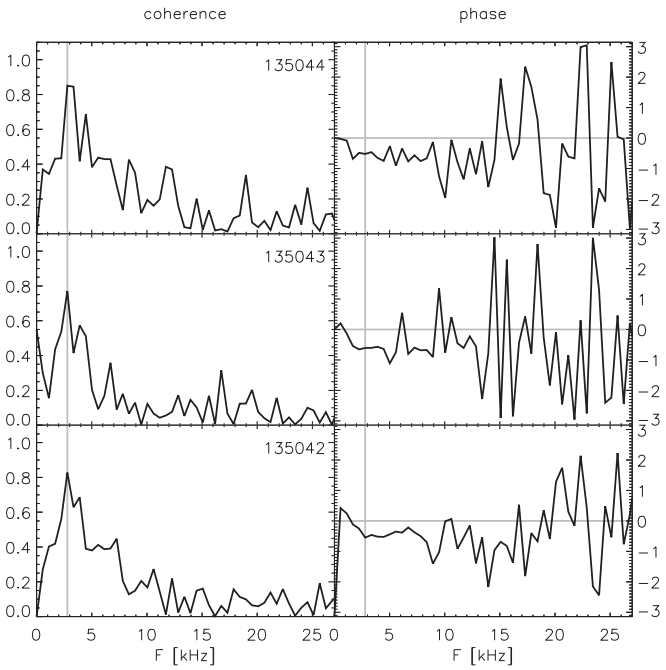

FIG. 7. Coherence and phase plots vs frequency for poloidal velocity signals separated by ~12 cm poloidally at ~1 cm inside the separatrix.

and 30 kHz. The 2.8 kHz mode has a correlation length of 56 cm which is significantly longer than the turbulent correlation length of ~4 cm. Figures 8 and 7 suggest that this poloidal flow oscillation near 3 kHz is a large scale coherent oscillation.

Figure 9 illustrates the radial dependence of the poloidal velocity power spectrum. The spectra for the mean-subtracted poloidal velocity between $t \approx 0.240$ and 0.243 ms are first norm-squared, and then averaged poloidally. The figure shows the spectrum at three radial locations at $x=-3.9$, 0.6, and 3.5 cm. A strong feature near 2.5 kHz is

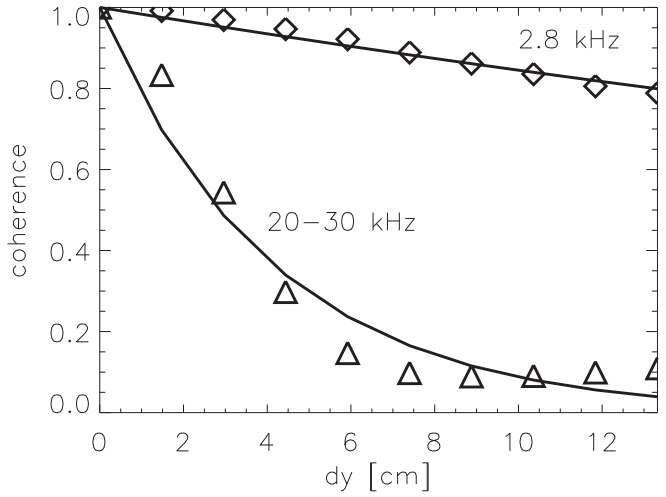

FIG. 8. Plot shows coherence of poloidal velocity vs y separation for 2.8 kHz mode (◇) and background turbulence between 20 and 30 kHz (△) for poloidal velocity of shot 135042. Velocities are measured at ~1 cm inside the separatrix. Solid lines are fits to exponential decays with correlation lengths of 56 cm for the 2.8 kHz mode and 4 cm for the background turbulence.

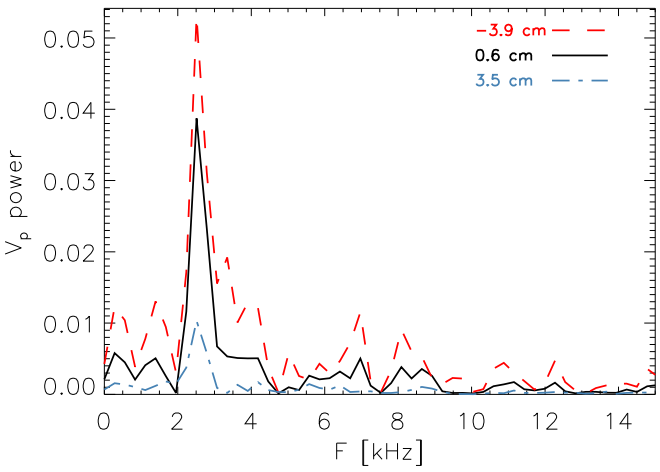

FIG. 9. (Color online) Autopower spectra of poloidal velocity at three radial positions for $t \approx 0.240-0.243$ s of shot 135042. The feature at 2.5 kHz does not appear to shift in frequency.

visible at the same frequency in the spectra at −3.9 and 0.6 cm, suggesting that the frequency of the mode does not depend on radius and hence temperature profiles. In addition, This feature in the poloidal velocity spectra is seen to extend a few centimeters into the SOL, but at 3.5 cm the feature is significantly reduced.

In summary, a strong feature near 3 kHz is observed in both the GPI and poloidal velocity spectra, and this feature exhibits a long poloidal wavelength in each case. In the radial direction, the 3 kHz flow oscillations outside the separatrix have a small negative phase shift relative to oscillations inside the separatrix. This phase shift indicates that the 3 kHz flow in the SOL slightly leads the flow inside the separatrix. Poloidal velocity fluctuations at 3 kHz also have a long correlation length that is an order of magnitude greater than the turbulence correlation length. In addition, the poloidal velocity fluctuations show no frequency variation between the separatrix and the inside edge of the view ($x \approx -4-0$), but the amplitude of the fluctuation decreases significantly inside the SOL.

VI. FLOWS, SHEAR, AND TURBULENCE

Turbulent flow properties, such as the shearing rate, $\langle dV_p/dr \rangle$, and the Reynolds stress, $\langle \delta V_p \delta V_r \rangle$, can be derived from the 2D flow field produced by the HOP-V algorithm. Here, $\delta V = V - \langle V \rangle$ and $\langle \cdots \rangle$ denotes a poloidal average unless otherwise noted. These quantities are important to the evolution of the turbulent system, and may partly control the strength of the turbulence and the transport of scalar quantities. The radial derivative of the Reynolds stress term is believed to drive the production of zonal flows via nonlinear energy transfer from drift wave turbulence,[2] thus leading to the suppression of drift wave turbulence and transport. Shearing of poloidal velocity is also thought to control turbulent transport via vortex stretching.[1,3,21]

To explore these relationships, F_{sol} is again plotted with poloidal velocity in Fig. 10, but also included here are the shearing rate and the turbulent Reynolds stress derived from the velocity field. Example traces of the Reynolds stress and

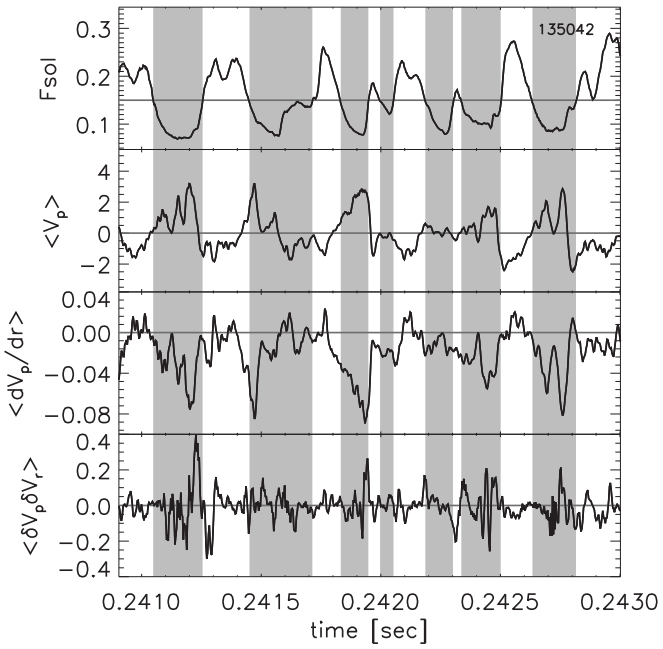

FIG. 10. Traces from shot 135042 of F_{sol}, poloidal velocity (km/s), shearing rate (MHz), and the Reynolds stress (km^2/s^2). Poloidal velocity and Reynolds stress are taken at ~1 cm inside the separatrix, and the shearing rate is taken at the separatrix. Traces have been smoothed with a three point boxcar average.

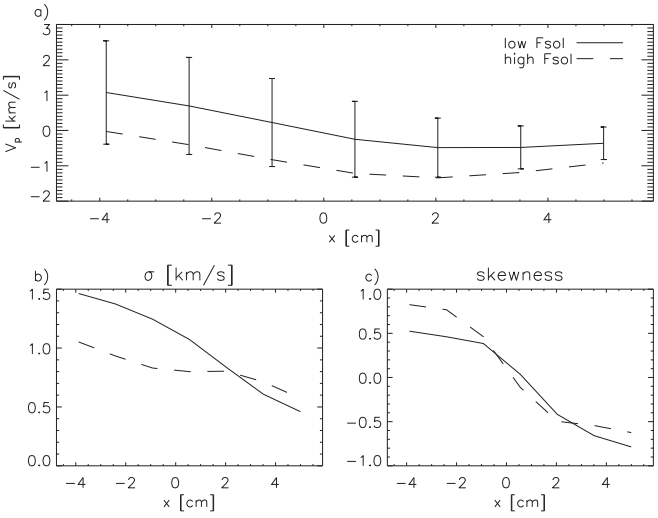

FIG. 11. Poloidal velocity profiles for ~30 ms of shot 135042 are plotted in (a). The averages are over times where F_{sol} is greater than its mean value (dashed—bursty) and less than its mean value (solid—quiet). Error bars indicate $\pm 1\sigma$ (standard deviation) about the average value for the low F_{sol} case, and indicate the level of fluctuation. Standard deviations are shown in (b), and skewness is shown in (c).

poloidal velocity are taken ~1 cm inside the separatrix to illustrate the time dependence of these quantities. Due to the shearing of eddies, one expects that flow shear localized to the area near the separatrix might suppress transport into the SOL,[3] thus Fig. 10 plots the shearing rate at the location of the separatrix. The plot covers 600 frames (~2 ms) of shot 135042 approximately 3 ms before the L-H transition. In addition to the correlated behavior of poloidal velocity with F_{sol} as described above, peaks in F_{sol} are correlated with periods when the shearing rate is near zero, and quiet periods are coincident with negative spikes in the shearing rate. For the time period shown, F_{sol} and the shearing rate are well correlated with a correlation coefficient of 0.53. This is consistent with a scenario in which the turbulence level is limited by the local shearing rate, as seen in recent simulations of the NSTX edge (Figs. (4) and (7) of Ref. 22). Almost all of the shots analyzed have short periods of ~2 ms where the correlation coefficient between F_{sol} and the shearing rate is greater than 0.4. Over longer time periods, however, the correlation values are much lower.

Figure 11 illustrates the differences in the poloidal flow profiles for times of high F_{sol}, bursty periods, and low F_{sol}, quiet periods, for ~30 ms of shot 135042. In Fig. 11(a) the dashed (solid) line is the poloidal flow profile averaged over times when F_{sol} is above (below) its mean value. Shots 135021–23 and 135041–45 all show a shift in the mean flow profile similar to Fig. 11(a). The shape of the profile does not appear to change significantly, indicating that the shear is similar in both cases. However, the entire profile is seen to shift ~1 km/s in the positive direction during periods of low F_{sol}. The "error bars" in Fig. 11(a) indicate ±1 standard deviation for the low F_{sol} average. These indicate the level of fluctuation about the mean value, and do not necessarily correspond to an uncertainty of the measured value. Also, The standard deviations [Fig. 11(b)] inside the separatrix are ~30%–50% greater during these periods. Therefore, during quiet periods we observe the mean flow becoming more positive, and, inside the separatrix, the fluctuations in the flow have a greater amplitude. The skewness profiles [Fig. 11(c)] typically do not show a significant difference during quiet periods, but some general characteristics may be observed. Inside the separatrix the skewness is positive, while outside the separatrix it becomes negative. Thus, inside the separatrix the distribution of measured poloidal velocities has a longer tail in the direction of more positive velocities, while the more negative tail of the distribution is longer outside the separatrix. This is consistent with our interpretation of Fig. 3 where we observed strong positive peaks in poloidal flow velocity during quiet times and strong negative peaks during bursts.

Recent SOL turbulence (SOLT) simulations[22] using parameters consistent with NSTX L-mode discharges found a parameter regime with large intermittent spikes of particle transport accompanied by quiescent periods of low particle transport. It was found that during the quiescent periods the shearing rate had a negative value, but crosses zero shear during bursts. For qualitative comparison, we include traces of F_{sol}, poloidal velocity, shearing rate (ξ), and Reynolds shear stresses from a SOLT simulation in the bursty regime (Fig. 12). Similar to Fig. 10, we see periodic bursts of F_{sol} at a frequency of 3.6 kHz accompanied by periods of low F_{sol}, quiet periods. F_{sol} exhibits strong correlation with poloidal velocity, and bursts are well correlated with the shearing rate, ξ approaching zero.

Figure 13 shows radial profiles of the Reynolds shear stresses for 10 ms sections of four shots preceding the L-H transition. Each profile has a local maxima near $x=-1$ cm,

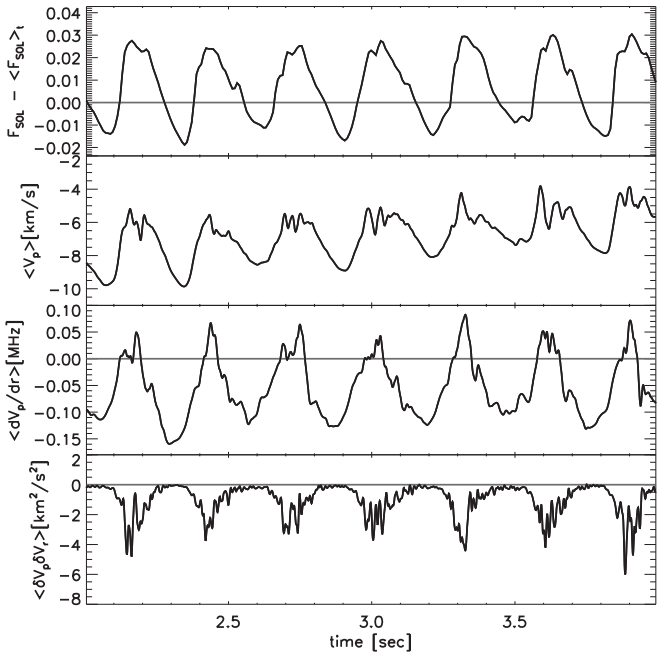

FIG. 12. Traces of F_{sol}, poloidal velocity (km/s), shearing rate (ξ), and the Reynolds shear stress. Traces are from a SOLT simulation illustrating the bursty regime. The frequency of bursts is 3.6 kHz.

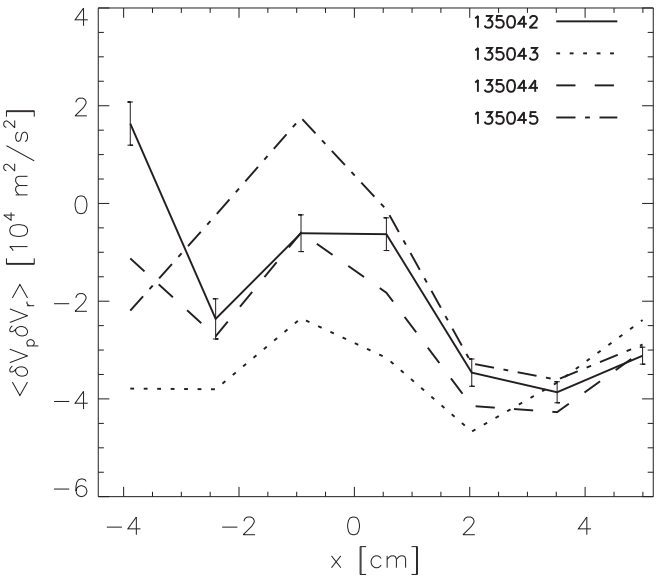

FIG. 13. Radial profiles of the Reynolds shear stress averaged over the poloidal direction and 10 ms directly preceding the L-H transition for four shots. Error bars indicate estimated level of uncertainty assuming uncertainties in the velocity measurements of 0.5 km/s.

negative slope between −1 and 2 cm, and a section of positive slope between −2 and −1 cm. The region of positive slope inside the separatrix is coincident with the region of poloidal flow shear seen in Fig. 1. Error bars have been added to the profile of shot 135042 assuming random, statistically independent uncertainties in the velocity measurements of 0.5 km/s (~0.5 pixel/frame). The Reynolds stresses may play an important role in the production of mean momentum from the turbulent velocity field. Areas with a finite radial gradient may be associated with the production or dissipation of poloidal momentum.

VII. DISCUSSION AND SUMMARY

Previously, Zweben *et al.*[13] reported on the observation of quiet, H-mode-like periods in the edge of NSTX preceding the L-H transition. The quiet periods are characterized by a decrease in the amount of D_α light in the SOL, and were observed to have a frequency of ~3 kHz. Poloidal velocity measurements were made using a time-dependent cross-correlation analysis. It was found that these quiet periods were correlated with reversals in the local poloidal flow and the dimensionless poloidal flow shear, and were less correlated with other turbulence quantities. The study sought a trigger to the L-H transition in the measured turbulence quantities, but found no systematic variation in these quantities preceding the transition.

In this paper, we examine the nature of the 2D turbulent flow field in the NSTX edge region during L-mode operation and the connection between the flow and the turbulence. Using the more complicated HOP-V analysis to extract velocities, we find that the turbulent bursts are strongly correlated with the poloidal flows and their radial shearing rate, which is in agreement with the analysis of Zweben *et al.* Beyond this, we characterize the spatial structure of the ~3 kHz flow oscillations, and find the ~3 kHz flow oscillations to be a large scale, coherent flow oscillation as described below. Also, we explore differences in the flow profile during periods of high and low F_{sol}, and we draw qualitative comparisons between observations and SOLT simulations. Finally, we report measurements of the Reynolds shear stresses in the edge region of NSTX.

One possible candidate for the observed periodicity is a GAM. The GAM arises from a coupling between sound waves and poloidal rotation induced by the toroidal curvature. These modes possess many general properties which can be compared to observable quantities: density fluctuations typically with poloidal mode number $m=1$ and toroidal mode number $n=0$, velocity fluctuations with $m=0$ and $n=0$, finite radial wavenumber, radial propagation, and frequency that scales with the sound speed and hence depends on $\sqrt{\gamma(T_e+T_i)/m_i}$ (γ being the adiabatic exponent). Recent calculations of GAM frequencies in NSTX using the NLET code[23] found several GAM candidates, and the lowest frequency mode was found on the same order as the 3 kHz oscillations.[13]

We observe strong features near 3 kHz in both the spectrum of GPI intensity and poloidal velocity, and both modes exhibit poloidal wavelengths on the order of meters. In addition, the correlation length for the poloidal velocity fluctuation at 3 kHz is found to be significantly greater than that of the background turbulence. Together, these points suggest that the flow oscillation is a large scale coherent fluctuation, which is consistent with the behavior of a GAM. However, we find that the frequency of the mode is independent of radius, the flow oscillations maintain their amplitude from the separatrix to the inside edge of the view, and the poloidal flow oscillations have only a small phase shift across the radial width of the view. Thus, we are unable to classify the

radial wavenumber, radial propagation, or the frequency scaling with temperature. Future work in this area would seek to clarify these points.

Recent simulations by the 2D SOLT code[22] identified parameter regimes characterized by intermittent, bursty particle transport. In these regimes, it was observed that shear flows acted to regulate the turbulent transport. In this paper, we report the qualitative similarity of these simulations with observations from NSTX, including strong correlations between turbulent bursts, poloidal flows, and flow shear. The simulations also exhibit periodic oscillations in turbulent bursts and poloidal flows similar to the 3 kHz feature seen in the NSTX data. The SOLT simulations do not include GAM physics, but do advance the zonal flows in the system using a zonally averaged poloidal momentum conservation equation. Thus the shearing of (non-GAM related) zonal flows, self-generated by the turbulence, offers an alternative explanation for the 3 kHz mode.

Another possible mechanism for driving the 3 kHz feature is the refilling of plasma along field lines. Periods of strong turbulent flux can eject large amounts of plasma, leaving the edge region depleted. Motion along the field lines will then refill the depleted region on the timescale $\tau=2\pi R/V_{\|}$, where R is the major radius of the device. For $T_i=T_e=50\ eV$ this yields a frequency of $f_{\|}\sim 7$ kHz, which is on the same order of magnitude as the observed fluctuations.

We have explored the relationship of flow shear and the flow profiles with the turbulence. We find periods (~ 2 ms) of good correlation between the turbulent bursts, seen in F_{sol}, and the shearing rate. Over longer time periods (~ 10 ms), however, the correlations are significantly reduced, and it appears that many things could complicate this relationship. It is possible that a minimum threshold value of shear is required to affect the turbulence. Also, low values of shear may not always trigger a turbulent burst; for example if a burst has happened recently. It is also possible that changes in the gradients of n_e and T_e throughout the shot could suppress or amplify the turbulence drive regardless of the shear levels. Thus, it should not necessarily be surprising that the correlations become significantly lower over longer time periods. Over these long time periods we do, however, see trends in the poloidal flow profiles. During periods of low F_{sol} the poloidal flow profile shifts in the electron diamagnetic drift direction ($+y$) by ~ 1 km/s, and the amplitude of flow fluctuations inside the separatrix, as described by the standard deviations, increases.

Finally, we report measurements of the radial profiles of the Reynolds shear stresses. Several shots have a similar Reynolds stress profile, with the stresses inside the separatrix possessing a positive radial gradient that is coincident with a region of negative mean poloidal flow and local flow shear. This is suggestive since turbulent shear stresses have been identified as a possible source for mean poloidal momentum. However, more analysis is required to demonstrate the transfer of energy from the turbulence to the large scale flows.

ACKNOWLEDGMENTS

We would like to thank K. Hallatschek, R. Hager, and the National Spherical Torus Experiment Team for their contributions to this work, which was supported by U.S. Department of Energy Contract Nos. DE-FG02-08ER54995, DE-SC0001966, and DE-AC02-09CH11466.

[1] P. H. Diamond, S.-I. Itoh, K. Itoh, and T. S. Hahm, Plasma Phys. Controlled Fusion **47**, R35 (2005).
[2] P. H. Diamond and Y.-B. Kim, Phys. Fluids B **3**, 1626 (1991).
[3] P. W. Terry, Rev. Mod. Phys. **72**, 109 (2000).
[4] A. Fujisawa, T. Ido, A. Shimizu, S. Okamura, K. Matsuoka, H. Iguchi, Y. Hamada, H. Nakano, S. Ohshima, K. Itoh, K. Hoshino, K. Shinohara, Y. Miura, Y. Nagashima, S.-I. Itoh, M. Shats, H. Xia, J. Q. Dong, L. W. Yan, K. J. Zhao, G. D. Conway, U. Stroth, A. V. Melnikov, L. G. Eliseev, S. E. Lysenko, S. V. Perfilov, C. Hidalgo, G. R. Tynan, C. Holland, P. H. Diamond, G. R. Mckee, R. J. Fonck, D. K. Gupta, and P. M. Schoch, Nucl. Fusion **47**, S718 (2007).
[5] A. Fujisawa, Nucl. Fusion **49**, 013001 (2009).
[6] K. Itoh, S.-I. Itoh, P. H. Diamond, T. S. Hahm, A. Fujisawa, G. R. Tynan, M. Yagi, and Y. Nagashima, Phys. Plasmas **13**, 055502 (2006).
[7] G. R. McKee, R. J. Fonck, M. Jakubowski, K. H. Burrell, K. Hallatschek, R. A. Moyer, D. L. Rudakov, W. Nevins, G. D. Porter, P. Schoch, and X. Xu, Phys. Plasmas **10**, 1712 (2003).
[8] J. L. Terry, S. J. Zweben, O. Grulke, M. J. Greenwald, and B. LaBombard, J. Nucl. Mater. **337–339**, 322 (2005).
[9] G. R. Tynan, P. H. Diamond, C. Holland, S. H. Muller, M. Xu, Z. Yan, and J. Yu, Plasma Phys. Controlled Fusion **51**, 124055 (2009).
[10] C. Holland, G. Tynan, G. R. Mckee, and R. J. Fonck, Rev. Sci. Instrum. **75**, 4278 (2004).
[11] D. K. Gupta, R. J. Fonck, G. R. McKee, D. J. Schlossberg, and M. W. Shafer, Phys. Rev. Lett. **97**, 125002 (2006).
[12] G. R. McKee, D. K. Gupta, R. J. Fonck, D. J. Schlossberg, M. W. Shafer, and P. Gohil, Plasma Phys. Controlled Fusion **48**, S123 (2006).
[13] S. J. Zweben, R. J. Maqueda, R. Hager, K. Hallatschek, S. Kaye, T. Munsat, F. M. Poli, A. Roquemore, Y. Sechrest, and D. Stotler, Phys. Plasmas **17**, 102502 (2010).
[14] S. Kaye, M. Bell, R. Bell, J. Bialek, T. Bigelow, M. Bitter, P. Bonoli, D. Darrow, P. Efthimion, J. Ferron, E. Fredrickson, D. Gates, L. Grisham, J. Hosea, D. Johnson, R. Kaita, S. Kubota, H. Kugel, B. LeBlanc, R. Maingi, J. Manickam, T. Mau, R. Maqueda, E. Mazzucato, J. Menard, D. Mueller, B. Nelson, N. Nishino, M. Ono, F. Paoletti, S. Paul, Y. Peng, C. Phillips, R. Raman, P. Ryan, S. Sabbagh, M. Schaffer, C. Skinner, D. Stutman, D. Swain, E. Synakowski, Y. Takase, J. Wilgen, J. Wilson, W. Zhu, S. Zweben, A. Bers, M. Carter, B. Deng, C. Domier, E. Doyle, M. Finkenthal, K. Hill, T. Jarboe, S. Jardin, H. Ji, L. Lao, K. Lee, N. Luhmann, R. Majeski, S. Medley, H. Park, T. Peebles, R. Pinsker, G. Porter, A. Ram, M. Rensink, T. Rognlien, D. Stotler, B. Stratton, G. Taylor, W. Wampler, G. Wurden, X. Xu, L. Zeng, and NSTX Team, Phys. Plasmas **8**, 1977 (2001).
[15] T. Munsat and S. J. Zweben, Rev. Sci. Instrum. **77**, 103501 (2006).
[16] S. Zweben, R. Maqueda, D. Stotler, A. Keesee, J. Boedo, C. Bush, S. Kaye, B. LeBlanc, J. Lowrance, V. Mastrocola, R. Maingi, N. Nishino, G. Renda, D. Swain, J. Wilgen, and NSTX Team, Nucl. Fusion **44**, 134 (2004).
[17] S. J. Zweben, R. J. Maqueda, J. L. Terry, T. Munsat, J. R. Myra, D. D'Ippolito, D. A. Russell, J. A. Krommes, B. LeBlanc, T. Stoltzfus-Dueck, D. P. Stotler, K. M. Williams, C. E. Bush, R. Maingi, O. Grulke, S. A. Sabbagh, and A. E. White, Phys. Plasmas **13**, 056114 (2006).
[18] D. Stotler, B. LaBombard, J. Terry, and S. Zweben, J. Nucl. Mater. **313–316**, 1066 (2003).
[19] D. Stotler, J. Boedo, B. LeBlanc, R. J. Maqueda, and Z. J. Zweben, J. Nucl. Mater. **363–365**, 686 (2007).
[20] J. S. Bendat and A. G. Piersol, *Random Data: Analysis and Measurement Procedures* (Wiley, New York, 2000).
[21] H. Biglari, P. Diamond, and P. Terry, Phys. Fluids B **2**, 1 (1990).
[22] D. A. Russell, J. R. Myra, and D. A. D'Ippolito, Phys. Plasmas **16**, 122304 (2009).
[23] K. Hallatschek and A. Zeiler, Phys. Plasmas **7**, 2554 (2000).